Pitfalls in the Interpretation of Delta Wing Flow Visualisation

Dr. D.I. Greenwell
Flight Management & Control Dept.
Mechanical/Sciences Sector, Room 57, B109
Defence Evaluation & Research Agency
DERA Bedford, Clapham, MK41 6AE, UK

Abstract

This paper illustrates some pitfalls in the interpretation of flow visualisation images of delta wing leading-edge vortices. Numerical simulations of tracer particle trajectories in around straight and helical vortices are presented, representing unburst and burst delta wing vortices respectively. For straight vortices, the appearance of the 'smoke-ring' effect in wind tunnel testing is analysed, and shown to be unrelated to the size or presence of a viscous inner core in the vortex. The role of the swirl-induced radial pressure gradient in the vortex centreline trace seen in water tunnels is demonstrated. For helical (burst) vortices, the crossflow topology visualised with upstream tracer injection is shown to depend on the vortex core size and the helix pitch. Typical vortex helices are close to a flow regime which can produce visualised flow structures resembling axisymmetric bubble breakdowns. It is postulated that the intermittent open-ended bubble burst seen in delta wing vortices is in fact an artefact of the tracer flow visualisation technique, as transient disturbances temporarily reduce the pitch of the fundamental helical burst structure.

List of Symbols

Conical vortex

a	edge of outer vortex core, $= r_0/x$
d_P	diameter of tracer particle
r, θ, x	cylindrical coordinates
r_e	equilibrium (smoke ring) radius
r_0	radius of outer core
u_F, v_F, w_F	axial, radial, tangential fluid velocities
U_0, V_0	freestream axial and radial velocity
α	Hall vortex swirl parameter
ϕ	swirl ratio, $= V_0/U_0$
ρ_P	tracer particle density
ρ_F	fluid density
μ	fluid viscosity
τ_V	viscous drag parameter
τ_P	density ratio, $= \rho_P/\rho_F$

Helical vortex

a_0	helix radius
C_{MS}	binormal velocity coefficient
C_{VT}	tangential velocity coefficient
k_0	helix pitch, $= p/2\pi$
p	helix pitch
r, θ, z	cylindrical coordinates
R, Ψ, Z	helical coordinates

Paper presented at the RTO AVT Symposium on "Advanced Flow Management: Part A – Vortex Flows and High Angle of Attack for Military Vehicles", held in Loen, Norway, 7-11 May 2001, and published in RTO-MP-069(I).

Report Documentation Page

Form Approved
OMB No. 0704-0188

1. REPORT DATE	2. REPORT TYPE	3. DATES COVERED
00 MAR 2003	**N/A**	**-**

4. TITLE AND SUBTITLE	5a. CONTRACT NUMBER
Pitfalls in the Interpretation of Delta Wing Flow Visualisation	5b. GRANT NUMBER
	5c. PROGRAM ELEMENT NUMBER
6. AUTHOR(S)	5d. PROJECT NUMBER
	5e. TASK NUMBER
	5f. WORK UNIT NUMBER
7. PERFORMING ORGANIZATION NAME(S) AND ADDRESS(ES) **NATO Research and Technology Organisation BP 25, 7 Rue Ancelle, F-92201 Neuilly-Sue-Seine Cedex, France**	8. PERFORMING ORGANIZATION REPORT NUMBER
9. SPONSORING/MONITORING AGENCY NAME(S) AND ADDRESS(ES)	10. SPONSOR/MONITOR'S ACRONYM(S)
	11. SPONSOR/MONITOR'S REPORT NUMBER(S)

12. DISTRIBUTION/AVAILABILITY STATEMENT
Approved for public release, distribution unlimited

13. SUPPLEMENTARY NOTES
Also see: ADM001490, Presented at RTO Applied Vehicle Technology Panel (AVT) Symposium held in Leon, Norway on 7-11 May 2001 , The original document contains color images.

14. ABSTRACT

15. SUBJECT TERMS

16. SECURITY CLASSIFICATION OF:			17. LIMITATION OF ABSTRACT	18. NUMBER OF PAGES	19a. NAME OF RESPONSIBLE PERSON
a. REPORT	b. ABSTRACT	c. THIS PAGE			
unclassified	**unclassified**	**unclassified**	**UU**	**16**	

R_Ω	Rossby Number, ≡ swirl ratio
U_∞	freestream velocity
V_B, W_B	induced binormal and tangential velocities
V_T	helix translational velocity
V_{tan}	crossflow tangential velocity
β	filament inclination from centreline
κ	curvature of vortex filament
Γ	vortex strength
σ	vortex core radius
τ	non-dimensional pitch, = k_0/a_0
Ω	helix rotational velocity

Introduction

The original impetus to the work reported here was given by Reference 1, which highlighted the potential for misinterpretation in dye flow visualization of unsteady 2D shear flows by taking a simple prescribed flowfield and using computer simulations of streaklines and timelines to demonstrate the appearance of spurious (but plausible) flow structures.

The wide range of flow topologies seen in the published literature on visualisation of delta wing vortices raised concerns that a similar phenomenon may be responsible for at least some of these apparent flow structures. For example, Figure 1 shows two typical delta wing flow visualisation images obtained using (a) smoke in a low-speed wind-tunnel [3] , and (b) entrained air in a high-speed water tunnel [4]. In the first, we see a tubular 'smoke ring' effect with a smoke-free void on the centreline, but in the second we see a well-defined marking of the vortex core. The 'smoke ring' radius is often equated to the edge of the viscous inner core found in delta wing vortices [5], but there is no experimental evidence for this hypothesis.

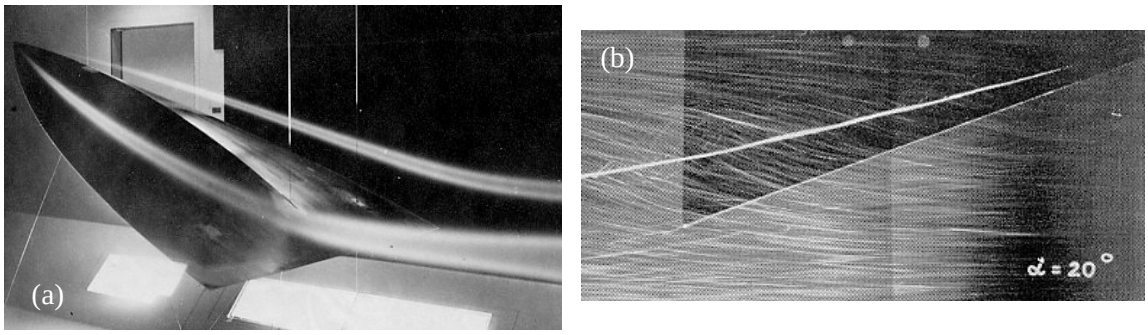

Figure 1 Typical vortex flow visualisation results using: (a) smoke in a wind tunnel [3], and (b) entrained air bubbles in a water tunnel [4]

As a start in addressing these concerns, this paper presents some results from an ongoing study of the effect of tracer particle characteristics on delta wing flow visualisation. The approach used is similar to that of Reference 1, using computer simulations of particle trajectories in prescribed flow fields approximating to those seen in delta wing vortices.

The first part of this paper deals with the effect of physical particle characteristics (eg mass and drag) on trajectories in a *steady-state* straight conical vortex. This work extends the little-known analysis of Reference 8 in order to elucidate the physical reasons for the differing images shown in Figure 1, and to demonstrate that there is no correspondence between the 'smoke ring' radius and the viscous core size. A more detailed description of the analysis and results of this section may be found in Reference 2.

The second part of this paper addresses the problem of flow visualisation for 'burst' vortices, with the analysis based on the hypothesis that the fundamental structure of a burst delta wing vortex is *helical* [6]. This hypothesis is based on flow visualisation studies that show that the 'spiral' form of vortex burst predominates for delta wing flows, particularly in wind tunnel experiments (Figure 2). On

occasions an axisymmetric 'bubble' burst is seen, but even here the internal flow within the bubble often displays a helical structure [7].

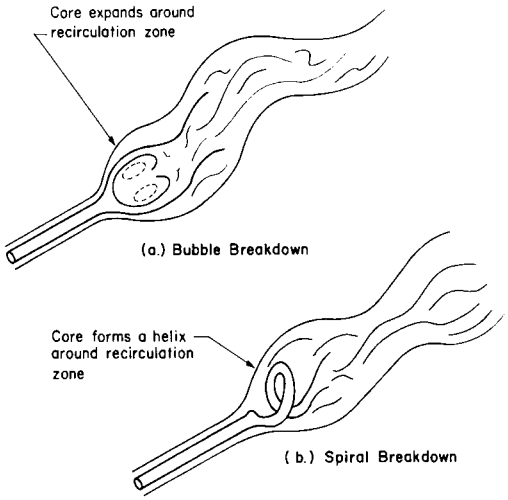

Figure 2 'Bubble' vs 'spiral' vortex breakdown [14]

As a first step, the *time-varying* burst vortex flowfield is modelled as a simple helical vortex of constant radius and pitch, undergoing self-induced translation and rotation [9]. This analysis yields an unexpected effect of the helix parameters on the cross-flow topology which may account for the intermittent appearance of an apparent 'bubble' burst in delta wing flows.

Visualisation in Conical Vortices

Conical Vortex Flow Model

A Hall vortex model [5] was used to represent the outer core of a conical leading-edge vortex, since this (a) gives a reasonable match to experimental data, and (b) unlike other popular vortex models specifies all three velocity components.

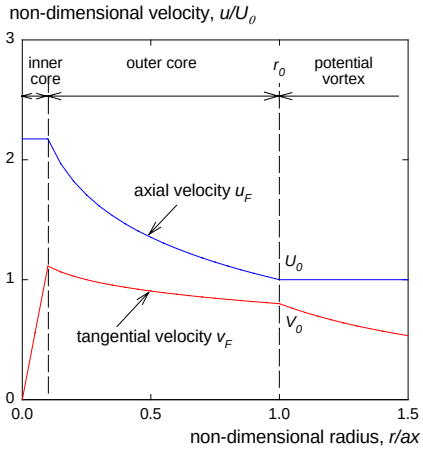

Figure 3 Axial and tangential velocity distributions in a Hall vortex, with swirl ratio $\phi_0 = 0.8$

The axial, tangential and radial fluid velocity distributions in the outer core region are:

$$u_F = U_0\left(1-\alpha\ln\left(\frac{r}{ax}\right)\right) \qquad (1a)$$

$$v_F = \left(V_0^2 - U_0^2 \alpha^2 \ln\left(\frac{r}{ax}\right)\right)^{0.5} \tag{1b}$$

$$w_F = -\frac{1}{2} U_0 \alpha \frac{r}{x} \tag{1c}$$

where U_0 and V_0 are the axial and tangential velocity components respectively at the edge of the vortex outer core (ie at $r_0 = ax$). α is the swirl parameter

$$\alpha = \left(1 + 2\phi_0^2\right)^{0.5} - 1 \tag{2}$$

where ϕ_0 is the swirl ratio V_0/U_0 at the edge of the vortex core. Outside of r_0, the flow is modelled as a simple potential vortex with constant axial velocity U_0, while for the purposes of this study the inner viscous subcore was represented as a simple forced vortex (see Figure 3).

Equations of Motion

Assuming that the tracer particles are small rigid spheres, the forces acting on them are the: viscous drag, lift, gravity, added mass (virtual inertia), hydrostatic pressure gradient, hydrodynamic pressure gradient (buoyancy), and the Basset force. However, for representative experimental conditions the majority of these can be ignored [2], leaving only the viscous drag and the hydrodynamic pressure gradient.

The viscous drag force was modelled using Stokes' Law, while the hydrodynamic pressure gradients can be derived directly from the Hall vortex model. The resulting equations of motion for a particle (in cylindrical coordinates) are [2]:

$$\ddot{x}_P = \frac{1}{\tau_V}\left(u_F - \dot{x}_P\right) + \frac{1}{\tau_P}\frac{v_F^2}{x_P} \tag{3a}$$

$$\ddot{\theta}_P = \frac{1}{r_P}\left(\frac{1}{\tau_V}\left(v_F - r_P\dot{\theta}_P\right) - 2\dot{r}_P\dot{\theta}_P\right) \tag{3b}$$

$$\ddot{r}_P = \frac{1}{\tau_V}\left(w_F - \dot{r}_P\right) - \frac{1}{\tau_P}\frac{v_F^2}{r_P} + r_P\dot{\theta}_P^2 \tag{3c}$$

where τ_V is a parameter relating centripetal force to drag force, defined as:

$$\begin{aligned}\tau_V &= \frac{d_P^2 \rho_P}{18\mu} \\ &\equiv \frac{\pi\left(d_P^3/6\right)\rho_P \omega^2 r}{3\pi d_P \mu r \omega}\frac{1}{\omega}\end{aligned} \tag{4a}$$

and τ_P is the particle/fluid density ratio:

$$\tau_P = \frac{\rho_P}{\rho_F} \tag{4b}$$

Typical Numerical Results

Figures 4 and 5 present some representative 3D simulation results for smoke particle trajectories around a conical leading-edge vortex flow at typical low-speed wind tunnel test conditions. Figure 4 shows the effect of conical particle injection along the edge of the outer vortex core, equivalent to smoke injection into the feeding shear layer (eg at the wing leading-edge).

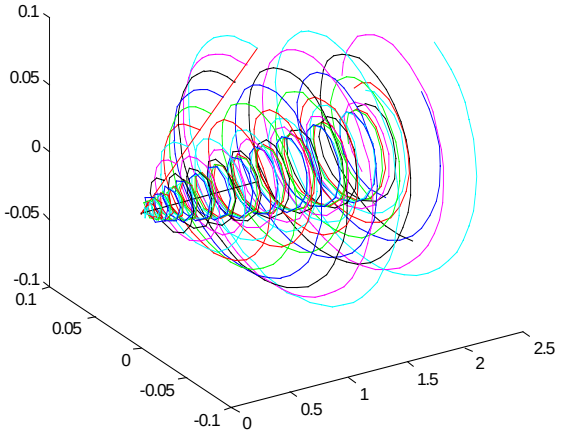

Figure 4 Tracer particle trajectories for conical particle injection at typical wind tunnel test conditions

The tracer particles appear to be spiralling inwards to form a ‘tube’ or ‘smoke ring’ effect similar to that seen in Figure 1a, with the smoke ring increasing in size downstream. The smoke ring effect can be seen more clearly in the right-hand side of Figure 5, which shows the particle distribution at a given chordwise point in terms of smoke density (relative to the seeding density).

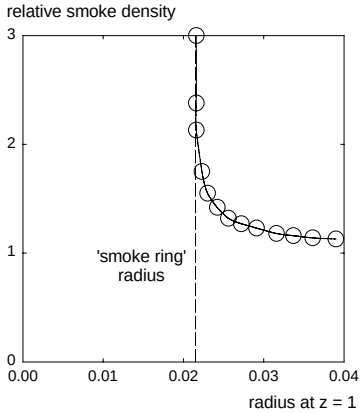

Figure 5 Relative smoke density in crossflow plane, showing the ‘smoke ring’ effect

Figure 6 presents some representative 3D simulation results for buoyant particle trajectories at typical water tunnel test conditions. In contrast to the wind tunnel results described above, no ‘smoke ring’ structure is seen. Instead, the tracer particles follow the true radial velocity component much more closely and migrate rapidly inwards to the vortex core where they accumulate. The particle density on the vortex centreline becomes very high, giving the clear core trace effect seen experimentally in Figure 1b.

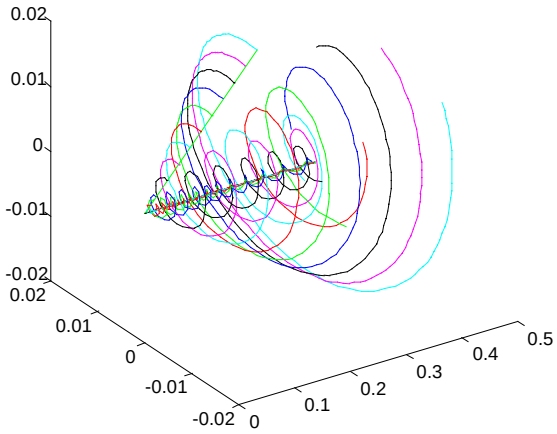

Figure 6 Tracer particle trajectories for conical particle injection at typical water tunnel test conditions

Simple 'Smoke Ring' Model

The tracer particles are in radial equilibrium (at $r = r_e$) when the radial force acting on the particle is zero. Assuming that (a) tangential and axial velocity following errors are generally small, (b) w_F is small in relation to U_0, and (c) outside the viscous inner subcore $u_F \approx U_0$, some manipulation of Equations (1), (2) and (3c) gives

$$\frac{dr_e}{dx} \approx \frac{\tau_V}{r_e} U_0 \phi_0^2 \left(1 - \frac{1}{\tau_P}\right) \tag{5}$$

Reference [8] uses a slightly different approximation to arrive at a similar equation, but neglects the $1/\tau_P$ radial pressure gradient contribution.

Equation (5) can now be integrated with respect to chordwise location x to find the equilibrium (smoke ring) radius

$$r_e \approx \phi_0 \sqrt{2x\tau_V U_0 \left(1 - \frac{1}{\tau_P}\right)} \tag{6}$$

Substituting for τ_V and τ_P from Equation (4) then gives

$$r_e \approx \phi_0 \frac{d_P}{3} \sqrt{Re_x (\tau_P - 1)} \tag{7}$$

where Re_x is the fluid Reynolds Number based on chordwise location x. Note that the vortex outer core radius factor a does not appear in Equation (6) or (7). Reference 2 shows that Equations (6) and (7) compare well with the results of full 3D tracer particle motion simulation, and are consistent with the limited experimental evidence available for smoke ring radii [8].

Hall's analysis [5] of the behaviour of the viscous inner subcore shows that

$$r_{inner} \propto \frac{x}{\sqrt{Re_x}} \tag{8}$$

Comparing this with Equation (7), it can be seen that the streamwise variation of the equilibrium radius r_e follows that of the viscous subcore r_{inner}, but that the variation with fluid parameters ρ_F and μ_F and with freestream velocity U_0 does not.

Implications of Model

The 3D simulations and simple model illustrate a number of pitfalls in the interpretation of smoke flow visualisation for straight conical vortices:

(a) The 'smoke ring' effect is independent of the presence (or size) of the viscous subcore.

(b) The variation of smoke ring radius with experimental parameters does not correspond to that of a viscous subcore, so cannot be used even as an indicator of the viscous core behaviour.

(c) The local 'smoke ring' radius is independent of the radius of the outer vortex core r_0 $(= ax)$.

The density ratio term $1\text{-}1/\tau_P$ in Equation (6) corresponds to the balance between radial pressure gradient and centrifugal forces. For typical smoke particles in a wind tunnel τ_P is large (of the order of 1000) and hence the particle density ratio has little effect on the smoke ring radius and can safely be neglected (as in Reference 8). However, if particle density is reduced towards neutral buoyancy (as for example in water tunnel testing) the $1\text{-}1/\tau_P$ term (and hence r_e) approaches zero and the radial pressure gradient effect can no longer be neglected. In this case the radial pressure gradient predominates and the tracer particles collect on the vortex centreline, giving the pronounced 'core marker' effect shown in Figures 1b and 6.

Equation (7) shows that for a given tracer substance, test Reynolds Number and incidence the smoke ring radius is directly proportional to particle diameter – emphasising the need to keep the size of 'heavy' particles to a minimum, particularly for optical measurement techniques (ie LDA or PIV) where the larger the smoke ring the larger the radial velocity following error will be. For buoyant particles the size will be less significant. Conversely, for given tracer particle characteristics and test Reynolds Number the smoke ring radius is directly proportional to swirl ratio (and hence to vortex strength), indicating that radial velocity measurement errors will increase with incidence.

Visualisation in Spiral Vortices

Spiral Vortex Flow Model

The flowfield and self-induced motion of a simple helical vortex of constant radius and pitch have been studied by many workers, who have generated as many different notations. The work reported here used elements from a wide range of numerical and theoretical studies, which unfortunately has resulted in a notation set which is not entirely consistent with the previous section.

We initially assume a fixed right-handed helix with radius a_0 and pitch $2\pi k_0$ (Figure 7a), with its axis in the z direction. In cylindrical coordinates the helix is represented parametrically as

$$r = a_0, \quad \theta = \phi, \quad z = k_0 \phi \tag{9}$$

The non-dimensional pitch is

$$\hat{\tau} = \frac{k_0}{a_0} = \frac{1}{\tan \beta} \tag{10}$$

where β is the local helix inclination to the centreline (positive for a right-handed helix). Figure 7b shows the normal, tangential and binormal unit vectors commonly used to define vectors relative to the vortex filament.

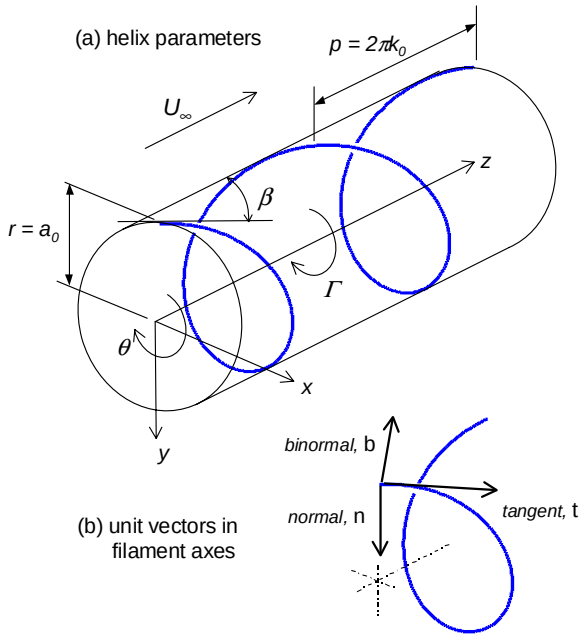

Figure 7 Helical vortex geometry and coordinate systems

The self-induced velocity component in the principal normal (radial) direction **n** is zero. The self-induced velocity in the binormal direction **b** is well-known [11] and is given by

$$V_B = \frac{\Gamma \kappa}{4\pi}\left(C_{MS} - \ln(\kappa\sigma)\right) \tag{11}$$

where Γ is the vortex strength, σ the radius of the vortex core and κ the filament curvature. The coefficient C_{MS} is a non-linear function of the non-dimensional helix pitch τ, with the majority of previous work on helix motion using a theoretical 'large pitch' approximation [11]. However, Kuibin [12] gives a semi-empirical curve-fit to his numerical results for intermediate values of the helix pitch.

The self-induced velocity in the tangential direction **t** (along the filament) is often ignored as not contributing to the overall helix motion, but may be of significance when considering vortex burst. This velocity is found to be independent of vortex core size, and is given by

$$W_B = \frac{\Gamma\kappa}{4\pi} C_{VT} \tag{12}$$

The coefficient C_{VT} is also a non-linear function of τ, for which a theoretical value for 'large' pitch can be extracted from Reference 11.

The flowfield induced by the helical vortex filament defined in Equation (9) was determined numerically using the Biot-Savart integral law, combined with a 'local induction approximation' for the core effects to avoid infinite velocities on the filament centreline[11]. Verification of the numerical method was provided by the comparison with theoretical values for the velocity coefficients C_{MS} and C_{VT} shown in Figure 8.

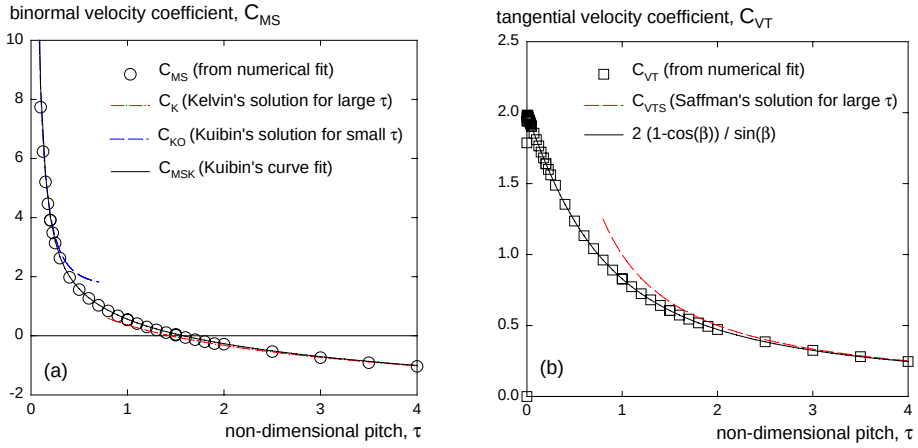

Figure 8 Effect of helix pitch on binormal, and tangential induced velocity components

Numerical experimentation established two preliminary results of some interest:

(a) Firstly, a remarkably good empirical fit to the tangential velocity coefficient C_{VT} is given by

$$C_{VT} = \frac{2(1-\cos\beta)}{\sin\beta} \tag{13}$$

This fit is so good as to suggest that there is some theoretical basis for it; however, this has yet to be investigated.

(b) Secondly, adding linear longitudinal variations in vortex strength Γ*(z)* and in helix radius $a_0(z)$ has no significant effect on the induced velocities given by Equations (11) and (12), if the *local* vortex and helix parameters are used. The following analysis should therefore apply equally well to a conical helix.

Transitions in the Cross-Flow Topology

As a result of the self-induced binormal velocity V_B, the helical vortex filament will translate and rotate with effective velocities [9]

$$V_T = V_B \sin\beta + U_\infty$$
$$\Omega = -\frac{V_B \cos\beta}{a_0} \tag{14}$$

where U_∞ is the longitudinal freestream velocity.

The flow-field induced by the vortex will therefore in general be time-varying. However, following the approach of Mezic et al [9] we can make a time-dependent change of coordinates from a cylindrical (r,θ,z) system into a helical (R,Ψ,Z) coordinate system which moves with the vortex, defined (for constant V_T and Ω) as

$$R = \frac{r}{a_0}$$
$$\Psi = (\theta - \Omega t) - Z \qquad (15)$$
$$Z = \frac{z - V_T t}{k_0}$$

for which the steady-state velocity field is a function of R and Ψ only.

The time-varying cross-flow streamlines induced by the vortex in the basic (r,θ) plane show no *qualitative* change when the helix parameters are varied; however Reference 9 demonstrates that in the time-shifted steady-state (R,Ψ) plane there are *three* distinct cross-flow topologies, depending on the helix pitch, radius and core size (Figure 9a).

Although at first glance this may seem irrelevant to the question of how tracer particles behave in and around a time-varying spiral vortex burst, it transpires that the cross-flow topology in the (R,Ψ) plane relates directly to the *instantaneous* cross-flow topology that would be observed in the $(r,\theta,)$ plane for tracer particles injected upstream, close to the unperturbed vortex core.

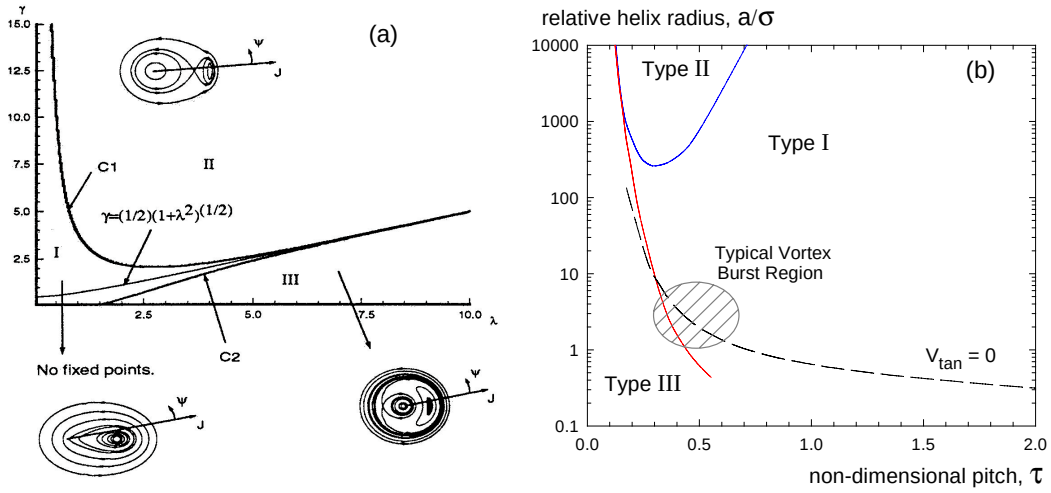

Figure 9 Transition diagram for the cross-flow topology in the R-Ψ plane: (a) from Reference 9, and (b) replotted as function of pitch τ and radius a/σ

Consider a single 'ideal' tracer particle released into a time-varying helical vortex flow at (r_0,θ_0, z_0), which traces a *pathline* $(r_p(t),\theta_p(t), z_p(t))$. This single particle pathline will not in general be either a *streamline* or a *streakline*[*]; however, it can readily be transformed into an equivalent instantaneous streakline emanating from an injection point rotating with the vortex. This situation would for example correspond to smoke injection into the vortex core region upstream of the burst point.

[*] a *pathline* is the track of a single fluid element, whereas a *streakline* is a curve joining the instantaneous positions of fluid elements which have passed through a given point, and a *streamline* is a curve normal to which the fluid velocity is instantaneously zero [10];.

Assume an injection point rotating with the vortex filament, so that r_0 and z_0 are fixed and

$$\begin{aligned}\theta_0'(t) &= \theta_0 + \Delta\theta_0(t) \\ &= \theta_0 + \left(\Omega - \frac{V_T}{k_0}\right)t\end{aligned} \tag{16}$$

thus allowing for both the rotational and the translational motion of the helix. The corresponding streakline at any given time t_{view} is then obtained from the original pathline $(r_p(t), \theta_p(t), z_p(t))$ by the rotation

$$\theta_s\left(z_p(t), t_{view}\right) = \theta_p(t) + \left(\Omega - \frac{V_T}{k_0}\right)\left(t_{view} - t\right) \tag{17}$$

Using a laser light sheet or equivalent we image the flow at time t_{view} at a given streamwise location z_{slice}. We denote the time the original tracer particle reached z_{slice} by t_{slice}, so that $z_{slice} \equiv z_p(t_{slice})$. From Equations (16) and (9) the instantaneous angular position of the vortex filament at z_{slice} is

$$\theta_v = \left(\Omega - \frac{V_T}{k_0}\right)t_{view} + \frac{z_{slice}}{k_0} \tag{18}$$

Subtracting Equation (18) from (17) then gives the instantaneous angular and radial positions of the streakline relative to the vortex filament as

$$\begin{aligned}\Delta\theta_s(z_{slice}) &= \theta_s(z_{slice}) - \theta_v \\ &= \theta_p(t_{slice}) - \left(\Omega - \frac{V_T}{k_0}\right)t_{slice} - \frac{z_p(t_{slice})}{k_0}\end{aligned} \tag{19a}$$

and

$$r_s(z_{slice}) = r_p(t_{slice}) \tag{19b}$$

which from Equation (15) is equivalent to

$$\begin{aligned}\Delta\theta_s(z_{slice}) &= \Psi_p(t_{slice}) \\ r_s(z_{slice}) &= a_0 R_p(t_{slice})\end{aligned} \tag{20}$$

In other words, for a given upstream tracer injection point rotating with the vortex helix, the trajectory (as z is varied) of the instantaneous $(r, \Delta\theta)$ crossflow position of the *streakline* relative to the helix therefore corresponds to a *pathline* in the helical (R, Ψ) crossflow plane.

Returning to Figure 9a, Mezic et al identify 3 classes of cross-flow topology in the (R, Ψ) plane, depending on the pitch and core size parameters λ and γ [9]. Type I topology is similar to that for a straight vortex, with closed orbits around the vortex core. Types II and III topologies have a second set of closed orbits about the centre of rotation of the helix. These types are distinguished by the position of the fixed point where the separating stream surfaces touch: for Type II this point lies on the axis between the vortex core and the centre of rotation (ie at $\Psi=0$), but for Type III the fixed point is opposite the vortex core at $\Psi=\pm\pi$.

Figure 9b shows the transition diagram of Figure 9a replotted in terms of the non-dimensional pitch τ $(=k_0/a_0)$ and the helix radius relative to the vortex core size, a_0/σ. The shaded region indicates typical helix parameters for burst delta wing vortices. The dashed line marked '$V_{tan} = 0$' indicates helices for which material elements have zero crossflow tangential velocity, where V_{tan} is given by

$$V_{tan} = W_B \sin\beta - V_B \cos\beta \tag{21}$$

There is some experimental [7] and computational [13] evidence that this is the case, at least in the early stages of a spiral vortex breakdown.

It can be seen from Figure 9b that:

(a) the Type II cross-flow topology is of theoretical interest only, being limited to unrealistically small cores (or very large radii).

(b) typical burst vortex helices lie very close to the Type I / Type III boundary.

Impact of Transition on Flow Visualisation

Tracer particles in a Type I flow behave as one might intuitively expect for a vortex flow, circling in an orderly fashion about the vortex core location. Conversely, tracer particles in a Type III flow display much more complex behaviour.

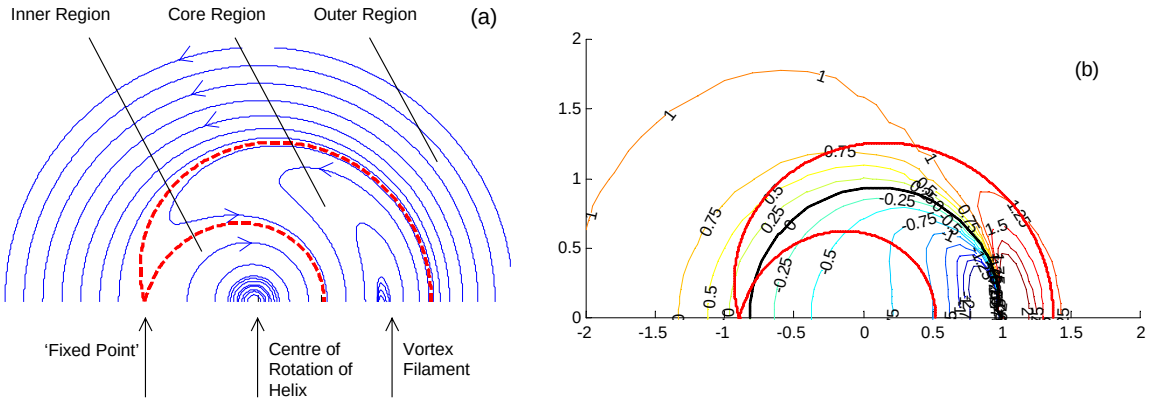

Figure 10 Typical Type III flowfield ($\tau = 0.24$, $a_0/\sigma = 2$, $R_\Omega = 0.8$): (a) crossflow streamlines in the R-Ψ plane, and (b) axial velocity contours relative to freestream velocity

This behaviour can be illustrated using a numerical example for a helix of non-dimensional pitch $\tau = 0.24$ (equivalent to a pitch p of $1.5a_0$) and radius $a_0 = 2\sigma$. The nominal vortex strength Γ and helix radius a_0 are –1.0 and 1.0 respectively, corresponding to a spiral of opposite hand to the vortex rotation [14]. An appropriate value for the freestream velocity U_∞ is obtained from the Rossby Number (or swirl ratio) parameter R_Ω, defined as

$$R_\Omega = \left| \frac{\Gamma}{2\pi\sigma U_\infty} \right| \tag{22}$$

Experimental studies indicate that delta wing vortex breakdown occurs at swirl angles of 40° to 50° [14], corresponding to critical Rossby Numbers of the order of 0.8 to 1.2.

This example generates the Type III crossflow streamlines in the (R, Ψ) plane shown in Figure 10a, where the dashed lines indicate the separating streamlines bounding the closed orbits around the vortex core and the centre of rotation. Figure 10b is a contour plot of the corresponding axial velocities relative to the freestream velocity given by Equation (22). The separating crossflow streamlines are highlighted, as is the zero axial velocity contour.

Recalling from Equation (20) that pathlines (and hence streamlines) in the steady-state (R, Ψ) plane correspond to the trajectories of streaklines in the time-varying $(r, \Delta\theta)$ plane, we can see from Figure 10 that the behaviour of tracer particles injected into this flow will depend critically on the injection position relative to the separating streamlines. These streamlines define three regions in the crossflow plane:

(a) *Inner region* – close to the centre of rotation. Particles injected into this region orbit about the centre of rotation in the opposite direction to the overall swirl velocity, and tend to move *upstream* due to the reverse flow induced by the spiral vortex near the helix centreline.

(b) *Core region* – centred on the vortex core. Particles injected into this region will orbit the vortex core. The axial velocity profile in this region is such that the particles tend to move slowly *downstream*, but with a cyclic fore-and-aft motion superimposed [9].

(c) *Outer region* – outside the helix. Particles injected into this region spread rapidly *downstream* and around the outside of the spiral vortex.

This behaviour is graphically illustrated in Figure 11, which shows downstream cross-flow slices for an initially concentric 'ideal' tracer injection pattern centred about the vortex core. The slices are viewed from upstream, so that the overall swirl direction is anti-clockwise. The injection pattern (11a) represents the 'smoke ring' phenomena described in the first part of this paper for a straight vortex, and was sized to cover all three regions listed above. Also indicated on Figure 11 are the separating cross-flow streamlines.

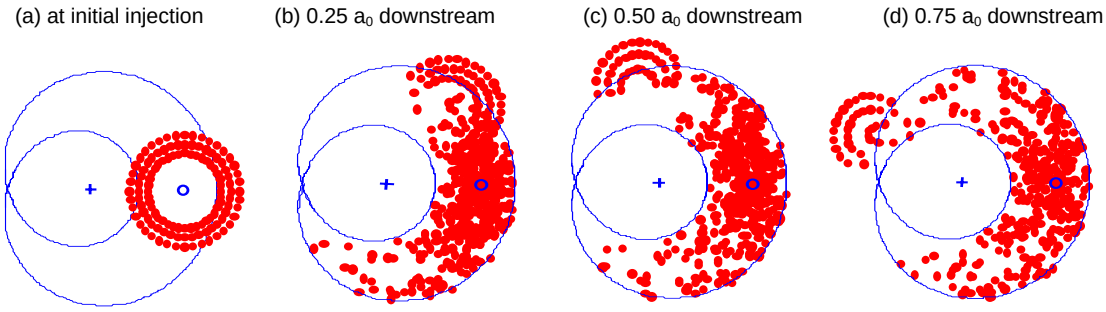

Figure 11 Cross-flow slices in the r-$\Delta\theta$ plane for an initially concentric injection pattern (Type III flow, 'ideal' tracer)

Reverse flows in the 'inner' region clear this portion of the flowfield of tracer particles. Conversely, the 'core' region rapidly fills up as we move downstream. This process is accelerated by the imposed cyclic fore-and-aft axial motion, since a particular streakline may pass through a given crossflow plane several times. Particles in the 'outer' region are swept round the outside of the helix in the direction of the vortex-induced swirl. For the particular injection pattern shown here, the tracer particles in the outer region are beginning to clump together into a apparent spiral of opposite hand to the vortex – a further example of the potential for seeing spurious flow structures in visualisation of unsteady flows.

For 'heavy' smoke-like tracers the behaviour in the outer region becomes of greater significance, because particles are centrifuged into it out of the vortex core region. This is illustrated in Figure 12 for tracer particle and fluid parameters representative of wind tunnel test conditions.

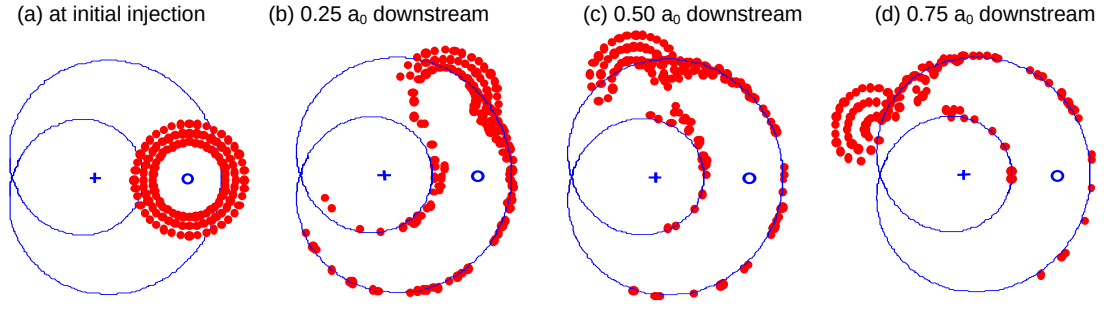

Figure 12 Cross-flow slices in the r-$\Delta\theta$ plane for an initially concentric injection pattern (Type III flow, 'heavy' tracer particles)

Overall, the emerging flow visualisation image is that of a cylindrical cloud surrounding a void on the helix centreline The spiralling vortex core is embedded within this cloud, but is not clearly visible. This structure in fact strongly resembles the 'bubble' burst phenomenon sometimes seen in delta wing vortex flows (Figure 2 [14]). Although Figure 9 suggests that typical vortex breakdown helices lie in the Type I flow regime, it appears likely that transient disturbances could temporarily 'compress' the

helix into the Type III region. Some experimental support for this hypothesis is given by the observation that 'bubble' bursts are often observed in dynamic pitching tests when the wing is pitching *up* - when aerodynamic time delays [16] give a vortex burst point *aft* of its equivalent steady-state location.

For confined vortex flows (eg in vortex tube experiments), axisymmetric 'bubble' breakdowns are stable, well-defined and well-documented. In contrast, 'bubble' breakdowns in unconfined delta wing vortices are unstable, poorly defined and differ considerably in their apparent structure from vortex tube results. In particular, bubble breakdowns in vortex tubes are *closed* (ie limited in their streamwise extent), while delta wing bubble breakdowns are *open-ended*.

The above analysis suggests that an alternative explanation for delta wing flows is that 'bubble' bursts may be simply be an artefact of the tracer flow visualisation technique in an unsteady flow. More work will be needed to confirm this, but some support is leant by recent PIV studies [eg 17] which to the author's knowledge invariably show spiral structures in the *instantaneous* flowfield of a burst delta wing vortex.

Summary

The simple numerical analyses presented in this paper have shown that many of the flow structures apparently seen in wind and water tunnel visualization studies of delta wing vortices may in fact be artefacts of the tracer particle flow visualisation technique itself.

Two flow cases were examined using 3D simulations of the paths of 'real' tracer particles: a steady-state straight conical vortex representing an 'unburst' leading-edge vortex, and an unsteady helical vortex representing a 'burst' vortex.

For the 'unburst' vortex, numerical simulation reproduced two classes of flow structures seen experimentally: tubular 'smoke rings' in wind tunnel test conditions, and vortex core tagging in water tunnel test conditions. A simplified analysis showed the smoke ring radius to be a function of the maximum swirl angle, the tracer particle diameter and relative density, and the Reynolds Number. The smoke ring radius was found to be independent of the size of the outer vortex core, and to be unrelated to the size (or indeed presence) of the inner viscous subcore.

At typical wind tunnel test conditions the smoke ring radius is large and dominated by the radial balance between viscous drag and centrifugal force, giving the potential for large radial velocity following errors in LDA or PIV measurements if particle diameters are not kept to a minimum. For dye flow visualisation in water tunnels the swirl-induced radial pressure gradient in the core dominates, giving smoke ring radii approaching zero and resulting in a clear indication of the vortex core centreline.

For the 'burst' helical vortex, the analysis is greatly simplified by transforming the unsteady flow into a helical coordinate system moving with the vortex. It is shown that pathlines in this steady-state coordinate system can be directly related to instantaneous streaklines emanating from an injection point rotating with the vortex. The critical feature of the flow in the time-shifted helical coordinate system is that there are three possible crossflow topologies, depending on the helix pitch and vortex core size. Typical burst vortex helices lie near to the boundary between a normal swirling flow centred on the vortex core (Type I) and a more complex topology with closed orbits about both the vortex core and the centre of rotation of the helix, surrounded by a normal swirling flow (Type III).

With a representative freestream velocity superimposed, axial velocities in the inner region centred on the centre of rotation of the helix are negative (ie reverse flow), but are positive in the outer swirling flow. In the vortex core region the mean axial velocity is positive, but there are areas of reverse flow. As a consequence, tracer particles in the inner region are convected upstream, tracers in the outer region are swept downstream and around the outside of the helix, while tracers in the vortex core region move more slowly downstream and spread into an arc centred on the core. If the particles are 'heavy' (eg smoke in a wind tunnel), then centrifugal forces rapidly clear out the core region.

Overall, the emerging flow visualisation image for a Type III helix is that of a cylindrical cloud surrounding a void on the helix centreline – a structure which strongly resembles the open-ended 'bubble' burst phenomenon sometimes seen in delta wing vortex flows. Assuming that transient disturbances could move a Type I burst vortex helix temporarily into the Type III flow regime, it is therefore postulated that an alternative explanation for intermittent 'bubble' bursts is that they are in fact an artefact of the tracer flow visualisation technique in an unsteady flow.

Acknowledgements

The work reported in this paper was carried out as part of a CRP Fellowship project, funded by the UK Ministry of Defence under Technology Group 3 of the Corporate Research Programme.

References

1. Gursul, I., Lusseyran, D. and Rockwell, D., "On Interpretation of Flow Visualization of Unsteady Shear Flows", Experiments in Fluids, Vol 9, 1990, pp257-266
2. Greenwell, D.I. and Gursul, I., "Effect of Tracer Particle Characteristics on Visualisation of Delta Wing Vortices", paper 111, 9th International Symposium on Flow Visualisation, Edinburgh, August 2000
3. Maltby, R.L. and Keating, R.F.A., "Flow Visualization in Low-Speed Wind Tunnels – Current British Practice", RAE Tech Note (Aero) 2715, August 1960
4. Elle, B.J., "An Investigation at Low Speed of the Flow Near the Apex of Thin Delta Wings with Sharp Leading Edges", ARC R&M 3176, January 1968
5. Hall, M.G., "A Theory for the Core of a Leading Edge Vortex", Journal of Fluid Mechanics, Vol 11, 1961, pp209-228
6. Jumper, E.J., Nelson, R.C. and Cheung, K., "A Simple Criterion for Vortex Breakdown", AIAA-93-0866, 1993
7. Lambourne, N.C., "The Breakdown of Certain Types of Vortex", NPL Aero Report 1166 (ARC 27200), September 1965
8. Maltby, R.L., Engler, P.B. and Keating, R.F.A., "Some Exploratory Measurements of Leading-Edge Vortex Positions on a Delta Wing Oscillating in Heave", ARC R&M 3410, July 1963
9. Mezic, I., Leonard, A. and Wiggins, S., "Regular and Chaotic Particle Motion Near a Helical Vortex Filament", Physica D, Vol 111, 1998, pp179-201
10. Stuart, J.T., Pankhurst, R.C. and Bryer, D.W., "Particle Paths, Filament Lines and Streamlines", NPL Aero Report 1057, March 1963
11. Saffman, P.G., "Vortex Dynamics", Cambridge University Press, 1992
12. Kuibin, P.A. and Okulov, V.L., "Self-Induced Motion and Asymptotic Expansion of the Velocity Field in the Vicinity of a Helical Vortex Filament", Physics of Fluids, Vol 10 No 3, March 1998, pp607-614
13. Visbal. M., "Computed Unsteady Structure of Spiral Vortex Burst on Delta Wings", AIAA-96-2074, 1996
14. Payne, F.M., Ng, T.T. and Nelson, R.C., "Visualisation of Leading Edge Vortices on a Series of Flat Plate Delta Wings", NASA CR4320, April 1991
15. Visser, K.D., "An Experimental Analysis of Critical Factors Involved in the Breakdown Process of Leading Edge Vortex flows", PhD Thesis, University of Notre Dame, April 1991
16. Greenwell, D.I., "Some Observations on the Dynamic Response to Wing Motion of the Vortex Burst Phenomenon", The Aeronautical Journal, Vol 98 No 972, February 1994, pp49-59
17. Shih, C. and Ding, Z., "Unsteady Structure of Leading-Edge Vortex Flow Over a Delta Wing", AIAA-96-0664, January 1996

Paper: #5
Author: Dr. Greenwell

Question by Dr. Luckring: As a comment, I think it would be interesting to consider using your model/analysis to assess the tube vortex breakdown results published by Liebovich & Fahler from Cornell (Physics of Fluids).

Answer: (No comment recorded.)

This page has been deliberately left blank

Page intentionnellement blanche